Ultrahigh-Resolution Colocalization of Spectrally Separable Point-like Fluorescent Probes

Xavier Michalet,[1] Thilo D. Lacoste,[2] and Shimon Weiss[1,3]

Material Sciences Division and Physical Biosciences Division, Lawrence Berkeley National Laboratory,
1 Cyclotron Road, Berkeley, California 94720

An ultrahigh-resolution colocalization method based on the simultaneous acquisition and analysis of spectrally separated images of the excitation point-spread function of point-like fluorescent probes is reviewed. It is shown that molecular distances can be measured with accuracy better than 10 nm using conventional far-field optics. A detailed account of the methodology, theoretical considerations, signal processing, and data fitting algorithms is given.   © 2001 Academic Press

Key Words: superresolution; diffraction limit; fluorescence; microscopy; confocal; two-photon; single molecule; TransFluoSphere; semiconductor nanocrystal; quantum dot.

Investigations of cellular substructures, relationship and dynamics of vesicles and organelles, and, ultimately, *in vivo* single-molecule interactions require microscopy techniques that can resolve the molecular scale. High-resolution imaging of biological samples (electron microscopy, X-ray microscopy) relies on natural contrast of the sample or on some organelle- or subcomponent-specific staining, either directly or indirectly (e.g., with labeled antibodies). However, differential labeling of multiple subcellular targets is not easy, and the number of different labels that can be detected in electron microscopy is limited. Last but not least, these high-resolution techniques require fixation of the sample, are destructive of the sample integrity, and are still too costly to be readily available to every researcher.

[1] Present address: Department of Chemistry and Biochemistry and Department of Physiology, University of California, Los Angeles, CA 90095.
[2] Present address: LifeBits AG, Albrechtstrasse 9, 72072 Tuebingen, Germany.
[3] To whom correspondence should be addressed. E-mail: Sweiss@chem.ucla.edu. Fax: (310) 206–4038.

Because it allows a larger variety of labeling schemes and because of its affordability, fluorescence microscopy has become the tool of choice for cellular imaging. However, except for aperture- and apertureless-near-field scanning optical microscopy (NSOM), the resolution of visible fluorescence imaging is usually limited by the diffraction of light (the "diffraction limit") to roughly half of the excitation or emission wavelength used. Significant efforts and technical developments are needed to go beyond this limit, that is, to be able to separate two point-like objects that are spaced apart by a distance shorter than the diffraction limit (the Rayleigh criterion). This limit is a major issue for studies that want to determine the localization of nanometer-scale objects in the cell, and ask for localization accuracy at least as small as the objects they are investigating.

Different approaches have been designed to go beyond the Rayleigh criterion. They can be classified in three types: (i) methods that involve significant modifications of the optical setup, (ii) methods that involve sophisticated processing of the acquired data, and finally, (iii) methods that resort to specific fluorescent probes or physicochemical processes for the generation of the recorded signal. In practice, all three types of modifications are combined in any given approach, but as often is the case, each method has its own set of constraints and a limited range of applications.

Here we detail a fluorescence colocalization method that allows the measurement of any distances between spectrally distinct probes with nanometer resolution. In Section 1, we review the main ideas and methods for colocalization measurements and the most promising attempts to improve resolution. In Section 2, we present the principles of our approach. Section 3 details the experimental setup and protocols. Section 4 is devoted to data acquisition and analysis, and discussion of the

resolution of this method. In Section 5 we report examples of distance measurements on fluorescent beads and semiconductor nanocrystals. Section 6 concludes with a discussion on prospects and future improvements.

1. STATE OF THE ART OF SUPERRESOLUTION FLUORESCENCE MICROSCOPY

In recent years, fluorescence microscopy has been the theater of major breakthroughs in terms of sensitivity, speed, and resolution. However, the variety of techniques and applications often makes it difficult to discern their real significance, differences, and ease of use. Below we subjectively attempt to sort out the different flavors of high-resolution fluorescence imaging and define criteria allowing for a fair comparison of sometimes unrelated techniques.

Excitation and observation of fluorescence can be achieved in three major historical ways: wide-field, confocal, and near-field scanning microscopy.

Wide-field fluorescence microscopy uses uniform illumination of the sample, such that the study of its resolution capacities is concerned only with the image of point-like light-emitting objects. This image is called point-spread function (PSF), which describes the three-dimensional (3D) energy density in image space (1). This distribution has typical sizes along the optical axis (about twice the emission wavelength along the optical axis) and perpendicular to it (about half the emission wavelength). In addition to the light emitted by the studied point, out-of-focus objects can emit light that will be collected and added to the signal of in-focus objects, leading to a general 3D blurring of details below the diffraction limit. However, imaging of incoherent light-emitting sources is a linear process, so that the image is in principle the superposition of images of infinitely many point-like sources (i.e., of infinitely many PSFs). Image processing techniques have thus been developed to recover the original distribution of point-like sources by inversion of this process, and are known under the generic name of "deconvolution techniques" (for a recent review, see Ref. (2)). Resolution down to 100 nm has been claimed by certain authors for 3D imaging (3, 4), but this necessitates intensive computation and does not eliminate the effect of aberrations (5).

An alternative approach to increase the imaging resolution of wide-field microscopy involves modification of the setup to modulate the excitation intensity (typically by interfering coherent light sources), to reduce the size of the illuminated region (6–8). Depending on the technique, resolution on the axial axis can go down to less than 100 nm (6, 7), or be improved in a perpendicular plane only to the same extent (8, 9). Finally, the optical system itself can be modified to modify the shape of the recorded PSF using superresolving filters (see, for instance, references in (10)).

All the above methods try to improve the separation of objects emitting at the same wavelength. For the simpler problem of distance measurement between point-like sources emitting at different wavelengths, these methods are not necessarily of any help. In this case, called here the polychromatic resolution problem (as opposed to the previously discussed monochromatic resolution problem), the question is merely to determine the position of the centers of well-defined intensity distributions (or PSF) obtained in separate acquisition channels. The practical limitations on position determination in a single channel are essentially the signal-to-noise level and the pixel size of the wide-field detector (typically a CCD camera), as we discuss in more detail later. Whichever method is adopted to determine the individual PSF's positions, a general agreement emerges to claim subpixel resolution (typically about 40 nm for visible wavelength) (11, 12). The low signal-to-noise ratio of fluorescence images does indeed not allow nanometer resolution to be achieved, as opposed to the case of transmission white-light microscopy of large beads, although the approaches are similar (13). Problems arise when information from different channels has to be combined to extract distance measurements, but we postpone this discussion to a later section of the article.

All these wide-field techniques suffer from contamination by out-of-focus point-like sources. This is practically eliminated in the confocal microscope design, which rejects out-of-focus light with the help of a pinhole at the objective's back focal plane. The image of a point source is now the product of the excitation and the emission PSFs, and has a smaller spatial extent, increasing slightly the intrinsic resolution of the microscope. Imaging resolution can thus be improved by the same set of methods that have been proven helpful in wide-field microscopy: deconvolution (14, 15), 4Pi (16) or PSF (17, 18) engineering, or superresolving filters (10). In addition, the use of an intense, short-pulse monochromatic laser source of suitable wavelength allows excitation of fluorescence via two-photon absorption (or higher-order multiphoton processes), giving some advantages in terms of specimen preservation from out-of-focus bleaching and sample penetration over standard one-photon confocal microscopy (19).

Despite these advantages, confocal microscopy does not eliminate aberrations coming from the different optical parts needed for excitation and emission light

transport. In particular, if one plans to use several excitation wavelengths, the most robust way to prevent difference in alignment is to couple all excitations through a common optical fiber and expand the beam just before entering the objective's back plane. Despite this precaution, wavelength-dependent properties of the objective lead to specific deformations of the different PSFs (20). Chromatic aberrations result in different z focuses for different wavelengths, and different PSF diameters, whereas spherical aberrations, coma, astigmatism, and uneven field flatness will result in problems for beams scanned off-axis. Finding the exact position of a point-like source under these conditions requires a thorough characterization of all these defects (5, 21–24).

A radical step to solve these issues is taken in near-field scanning optical microscopy (25–34) (for a recent review, see (35)), where the objective is eliminated altogether in the excitation path, replaced by an apertured or apertureless probe in direct or nearby contact with the sample. Although aberrations of the type described previously are eliminated, this technique suffers from several limitations: it is relatively difficult to implement, it is limited to surface investigations, and the PSF shape is still wavelength dependent and not well characterized, even though its spatial extent is significantly smaller than the confocal one (34).

In conclusion of this brief survey of fluorescence techniques available for superresolution imaging or distance measurement between point-like sources, we note that several additional constraints arise if one is interested in single-molecule imaging. Although they might appear to be the ideal point-like sources, they emit comparatively very few photons and are prone to various (photo)-chemical degradation reactions, which calls for very low background imaging conditions, very high sensitivity detectors, and relatively long acquisition times.

Finally, we have to mention that for the study of single molecules in contact with one another, or intramolecular distances, fluorescence resonant energy transfer (FRET), another approach limited to extremely short-range distances (1–10 nm), has to be considered (see other articles in this issue and Ref. (36)).

2. ULTRAHIGH-RESOLUTION COLOCALIZATION OF MULTICOLOR FLUORESCENT PROBES USING A SINGLE EXCITATION WAVELENGTH

The method we proposed recently for ultrahigh-resolution colocalization of multicolor fluorescent probes (37) is aimed at circumventing one of the previous limitations, namely, chromatic aberrations in the excitation path and, more generally, all problems arising from the use of several excitation wavelengths and various optical aberrations of far-field optics. Its principle is illustrated in Fig. 1 and is based on a single common excitation for all observed probes and the use of a closed-loop stage-scanning confocal microscope.

2.1. Description of the Method

First, this method is based on sample-scanning confocal microscopy using a single laser excitation wavelength and a closed-loop piezo-scanner (CLPS) that allows nanometer accuracy steps. In this design, each fluorescent probe is moved through the fixed electromagnetic field at the focal point of the objective lens, which is a diffraction-limited intensity distribution known as the PSF. A pixel-by-pixel map (image) of the excitation PSF is then built from the recorded fluorescence intensity of this probe.

Second, the method takes advantage of point-like fluorescent probes (i.e., much smaller than their emission wavelength) that can all be excited by the same laser wavelength but differ in their emission properties. The fluorescence of the different emitters needs to be separable or recorded independently in "orthogonal" channels. This separation can be based on differences in emission color, fluorescence lifetime, or any other photophysical characteristics. Examples of such point-like probes that were used in this study are small Trans-FluoSphere (TFS) beads (Molecular Probes, Eugene, OR; 40 nm in diameter) or semiconductor nanocrystal (NC) quantum dots (less than 10 nm in diameter). Since the same laser, aligned on the optical axis, excites all probes, differences in chromatic aberrations in the excitation path are altogether eliminated. This fixed-excitation scheme also ensures the equivalence of each channel in the detection path. As the sample consisting of these distinguishable probes is scanned through the
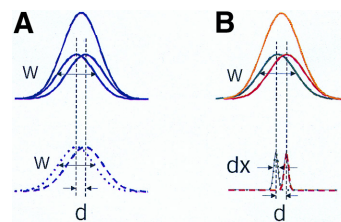
FIG. 1. Principle of ultrahigh-resolution colocalization. (A) When two point-like probes emit at the same wavelength, their overlapping signal cannot be resolved without further information if their distance d is smaller than about half the PSF's width W. (B) If the two point-like probes can be distinguished by their spectral fluorescence emission characteristics, the positions of their individual PSF images' centers can be determined with subpixel resolution dx, yielding an equivalent precision in their distance measurement.

excitation PSF, images are constructed pixel-by-pixel from the recorded signal of each channel. In these images, all pixels corresponding to a given nanometer-accurate scanner position are in perfect registry. Each individual point-like source will appear in one channel only as a diffraction-limited shape, identical to that of the excitation PSF.

Third, the resulting PSF images are fitted to a 2D gaussian function, a good approximation of the theoretical shape of the PSF. This allows one to localize their centers with the precision of a few nanometers, limited only by shot noise, photophysical noise of the fluorescence signal (triplet states, blinking, photobleaching), and electronic and mechanical noise of the piezo-scanning device. The distance of fluorescent emitters recorded in orthogonal channels can thus be determined with nanometer accuracy, a result we call ultrahigh-resolution colocalization (UHRC). The physical size of the probes is the lower boundary of the distance measurement; the upper boundary is given by the scan range of the piezo-scanner (here, 100 μm).

2.2. A Single Excitation Wavelength

As we discussed previously, two major problems are encountered when using several excitation wavelengths: chromatic aberrations in the excitation path, and sequential acquisition of the different channels.

One way around them is to get rid of far-field optics altogether for the excitation path, using a NSOM tip (38) for illumination and spectrally separated fluorescent samples. In this approach, all excitation wavelengths are brought to the sample via a small aperture, which ensures precise colocalization of the excitation sources. By scanning the excitation probe over the sample, multichannel emission data can be recorded simultaneously and remain in perfect registration. The resolution of the technique is in principle on the order of the aperture size (~100 nm). Cell surface images and membrane protein colocalization can be obtained with the above resolution, in addition to topography, as was illustrated on malaria-infected red blood cells in Refs. (39, 40). The method, however, is not very user-friendly, is almost impossible to operate in liquids, is invasive, and exhibits a nonlinear relationship between excitation and emission due to metallic tip–fluorophore interactions.

The gain in spatial monochromatic resolution of fluorescence NSOM compared with confocal microscopy can already reach one order of magnitude. However, much higher multispectral resolution can be obtained, as was described theoretically by Betzig for NSOM imaging of immobilized molecules (41), if the individual molecules

to be resolved spatially can be distinguished spectrally.[2] In this case, their emitted signal can be isolated in separate channels, and the task of finding their position is reduced to finding the center of the isolated PSFs. Betzig predicted uncertainties on the position measurement of individual terrylene molecules embedded in a polymer matrix of about 1 nm, using a a 40-nm aperture tip and scanning steps of 10 nm. As was illustrated by Ha *et al.* using two excitation beams coupled in a single fiber (see Figs. 2a and 2e), single-molecule multicolor imaging by NSOM is indeed feasible, but the shape of the PSF can vary from molecule to molecule due to different dipole orientations and tip–molecule interactions.

Even if very high resolution has been obtained (for instance, see Refs. (33, 34)), NSOM techniques are limited to surface studies and impose severe constraints on the type of samples that can be studied. Ideally, one would like to use far-field optics and a single excitation

FIG. 2. Advantages of using a single excitation wavelength. (A, E) In NSOM, two or more excitation wavelengths are brought simultaneously in close contact to the sample, yielding a very localized excitation volume (of typical size the diameter of the aperture, W). The probes need to have reasonably well-separated excitation and emission spectra. The resolution in position measurement is limited by the precise knowledge of the probe and location-dependent excitation volume's shape. (B, F) In using probes that have a broad excitation spectrum (like semiconductor nanocrystals), or can be excited by a single wavelength, the resolution in their distance measurement is limited only by the precision with which their separately recorded PSF images can be located. (C, F) The same principle applies for two-photon excitation. (D, F) Multicolor colocalization of different probes requires well-separable emission channels for each individual species.

[2] Ten years before, Burns *et al.* had proposed a similar idea for far-field imaging, using deconvolution of the acquired images (49). However, their method required acquisition of complete spectra for each data point. Their simulations gave a resolution about 50 times better than the Rayleigh criterion for a SNR of 15 dB (SNR = 5.6).

wavelength and be able to excite different probes that would differ from one another by recordable emission characteristics.

Resorting to far-field confocal optics, several schemes based on a single excitation wavelength can be envisioned, as illustrated in Figs. 2B–2D and 2F. They all rely on the availability of probes that can be distinguished by their emission properties and have a common excitation wavelength.[3] The first one uses direct excitation of fluorescence by one-photon absorption, and relies on the photophysical properties of the different probes to, for instance, reemit light with different Stock shifts (Fig. 2B). Such probes have been developed only recently, and we know of at least three types: semiconductor nanocrystals (NCs) (42–44), TransFluoSphere beads (TFSs), and energy transfer dye molecules (45). Of course, other characteristics besides emission wavelength could be used, as, for instance, fluorescence lifetime (46). The second solution consists of using two-photon excitation of different fluorophores (Fig. 2C). In this case, normal dyes can be used and it has been shown that single-molecule imaging is feasible (32, 47, 48; T. Her *et al.*, submitted). In case a complete spectrum is recorded for each pixel, one effectively ends up with a sample image in a $d + 1$ dimensional space, where d is the number of scanned spatial dimensions (49, 50), allowing the analysis of multicolor colocalization (Fig. 2D).

2.3. Stage-Scanning Confocal Microscopy

The UHRC approach can in principle be used with all kinds of confocal microscopes. We chose stage-scanning confocal microscopy for several reasons. Accurate (nanometer) localization of small beads/NCs requires sufficient signal-to-background/signal-to-noise ratios of the acquired fluorescence PSF data; i.e., relatively long (milliseconds to tens of milliseconds) integration times per pixel are needed. Galvanometers used for beam scanning do not perform well at such low frequencies. Also, in the stage-scanning design, the excitation PSF is fixed on the optical axis, eliminating uneven field-flatness and other off-axis aberrations introduced by the optical components. Moreover, closed-loop stage scanners perform better in terms of long-term stability of the calibration (they are more massive and protected than their beam-scanning counterparts), control over

step size, and reproducibility over large scan range. Their drawback, of course, is that they are much slower compared with beam-scanning galvanometers and are not suitable for video-rate imaging.

3. EXPERIMENTAL PROTOCOLS AND SETUP

3.1. Sample Preparation

Samples were prepared as described in Ref. (37). Briefly, 170-μm-thick glass coverslips were cleaned with acetone, methanol, and deionized water and treated with 1 M KOH in a sonicator for 30 min, rinsed in deionized water, and dried under nitrogen flow. TFSs 40 nm in diameter (excitation/emission peaks: 488/560 and 488/685 nm) were diluted in deionized water to 10^{-3} to 10^{-4} the stock concentration. A 10-μl drop containing a mixture of the two beads was left to dry on a coverslip in a desiccator and used immediately. Different NC batches (ensemble peak emissions: 540, 575, 588, and 620 nm) were prepared as previously described (51), mixed, and diluted in butanol before use. We routinely synthesized NCs with a full-width half-maximum (FWHM) ensemble spectrum of 30–40 nm. Each batch typically had ~5% variations in size as measured by transmission electron microscopy (51). Sample preparation was identical as for TFSs.

3.2. Optical Excitation and Scanning-Stage Setups

Two custom confocal setups (Fig. 3) using argon laser sources (Melles Griot) and optical microscopes equipped with oil immersion Plan-Apochromat ×100 (NA 1.4) objectives were used. Laser intensity (488 nm, linearly polarized) was recorded and feedback-controlled, ranging from 50 nW to 1 μW as measured in front of the dichroic beam splitter (505DRLP, Omega Filters), or equivalently from 80 W/cm^2 to 1.5 kW/cm^2 peak irradiance (52). The first setup comprised an Axiovert S100TV inverted microscope (Zeiss) and an open-loop flat piezo-scanner (NIS-30, Nanonics). The second consisted of an Axioskop 50 upright microscope (Zeiss) and a closed-loop, three-axis, piezo-scanning flexure stage equipped with capacitive sensors for position measurement (P-517.3CL, Physik Instrumente). The scanners were controlled by analog output boards (ATAO6, 12 bits and PCI 6111E, 12 bits, National Instruments) and homemade software written in C++ and LabVIEW (National Instruments), respectively. Scanned areas ranged from 1 × 1 to 10 × 10 μm^2, in steps of 25 to 100 nm, with integration times of 5 to 200 ms depending on the detector used. The CLPS was calibrated at the

---

[3] In the special case where different probes can be excited individually by different but very close excitation wavelengths (within 1/100 Å), and emit at the same wavelength, the effects of chromatic aberrations can also be safely neglected. van Oijen *et al.* have taken advantage of this to study the colocalization of individual pentacene molecules embedded in a *p*-terphenyl matrix at cryogenic temperature (65, 66) using wide-field imaging.

factory (1-nm accuracy); scanner positions were recorded at 10 kHz during each acquisition using a 12-bit analog input board (PCI 6111E, National Instruments).

3.3. Fluorescence Detection

Dual-color colocalization measurements (NCs and TFSs) were performed on the Axioskop (Fig. 3). A dichroic mirror (565DRLP for NCs and 610DRLP for beads, Omega Filters) separated green and red wavelengths onto two avalanche photodiodes (APD, SPCM AQ141), (EG&G, Perkin Elmer, Norwolk, CT), which simultaneously counted the photons on both channels. Bandpass filters in front of each APD minimized cross talk of both channels (535DF35 and 625DF25 for NCs, and 555DF25 and LP695 for TFSs, Omega Filters). Individual photon arrival times were recorded with a fast time-counting board (12.5-ns resolution, PCI 6602, National Instruments) and attributed online to each pixel of the dual-color image.

For multicolor colocalization work with more NCs, one costly option is to successively split the different colors by optical filters and use a large number of APDs. Instead, we designed a new apparatus (Fig. 3, lower right) incorporating a custom single-prism spectrometer (fused silica isosceles Brewster prism with AR coating, CVI Laser Corp.) in the detection arm of the Axiovert. The dispersed photons were projected onto a Peltier-cooled intensified charged-coupled device (ICCD) camera (PentaMax, Princeton Instruments). A limited area of the camera detector was selected, which encompassed the dispersed emission PSF. The camera was run in continuous triggered mode: at each piezo-stage step, the scanning controller board output a TTL pulse toward the camera, which triggered integration over the selected area for a prescribed duration. The resulting image was binned along the direction perpendicular to the dispersion axis (effectively reducing each individual PSF image to its profile), and dumped to the hard disk. A full spectrum (typically 270 data points)
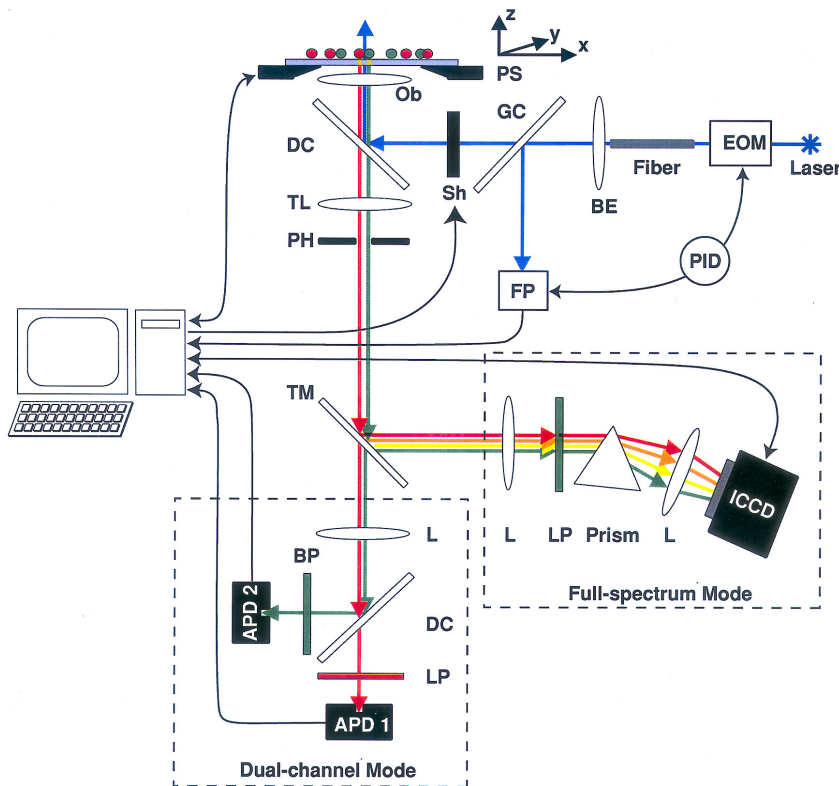
FIG. 3. Setup used in these experiments. Two types of microscopes were used. We only represent here the inverted setup, equipped with an open-loop piezo-scanner (no readout of the piezo-stage position was available contrary to what is indicated on the diagram). Two recording modes are possible: two-channel APD recording (Dual-Channel Mode, lower part) or full-spectrum ICCD recording (Full-Spectrum Mode, right-lower part). The upright microscope setup (same optical configuration except for the ICCD part) was equipped with a closed-loop piezo scanner, but no ICCD. EOM, electrooptical modulator; BE, beam expander; GC, glass coverslip; FP, fast photodiode; PID, feedback loop for the regulation of excitation power (SPM-100, RHK); Sh, shutter; DC, dichroic mirror; Ob, objective; PS, piezo stage. TL: Tube lens. PH: Pinhole. TM: Tiltable mirror. L: lens. LP: Long-pass filter. BP: Band-pass filter. Black lines indicate electronic links; arrows indicate the direction in which signals are transmitted.

was thus recorded for each image pixel in synchronization with the piezo-scanner movements. Calibration done with known laser lines showed a spectral resolution of 2 nm. Data acquisition was performed using WinView software (Princeton Instruments), with integration times ranging from 20 to 100 ms per pixel.

4. DATA ANALYSIS

All steps of the data analysis were performed using custommade software written in LabView and C. The next sections describe the different steps involved in the analysis.

4.1. Isolation of Spectral Channels

In the dual-channel acquisition mode (lower part of Fig. 3) two-color APD images were constructed by overlaying the two independent, false-colored channel images. In the full-spectrum mode (lower right part of Fig. 3), the 3D data set (one spectral + two spatial dimensions) had to be reduced in individual channel images for easier manipulation. Although sophisticated spectral analysis methods have been devised (see, for instance, Ref. (53)), we found out that a much simpler approach was able to detect individual spectra of many single NCs. Briefly, we scanned the spatial recording and summed the 10-nm binned spectra of each block of $n \times n$ pixels, where n is chosen in such a way that the block covers an area corresponding to the PSF extension. We summed these histograms and used the spectral peaks observed in the resulting histogram as central wavelengths for the filtering step. In the next step, spectral bands (typically 25 nm in width) centered around the previously extracted peaks were used to generate images from the original data set. From these images, the binned spectra of detected NCs were determined as explained previously, with the block of pixels centered on the approximate position of the observed NCs. It was found that the FWHM of the emission spectrum of a single NC was only 15–25 nm (see Fig. 4A, part a). In the third step, narrower spectral bands (5–20 nm) were chosen to define new color channels (Fig. 4A, part b) with reduced spectral overlaps (i.e., as "orthogonal" as possible). This procedure also allows one to examine the spectral inhomogeneities of NCs within a single batch.

In the fourth step, the above images were combined into a composite false-color image with perfect registry between each color plane (Fig. 4A, part c). These composite images obtained on the Axiovert setup (ICCD detection) are the multicolor equivalents of the dual-color images obtained on the Axioskop setup (APD detection). The final steps of the UHRC analysis were performed on dual-color images obtained with the Axioskop only, for it was the only one equipped with a CLPS.

4.2. Fitting Procedure

The fitting algorithm we used is a 2D generalization of the standard Levenberg–Marquard algorithm for χ^2 minimization of a nonlinear function, written in LabView. The minimized function is a 2D gaussian (possibly elliptical and tilted), including the background level as a fitting parameter (for a similar approach in 3D, see Ref. (54)). In addition to the usual χ^2 convergence criteria, we added a constraint on the variation of the fitted parameters, which we fixed at 10^{-4}, after we observed incomplete convergence for the mere $\Delta\chi^2 < 10^{-4}$ condition. Initial guess coefficients are either given by the user or determined by a linear minimization method (matrix method). The minimization is done in two steps: the first step assumes an equal weight for all selected pixels, which helps find a reasonable set of fitting parameters. The second step uses the same pixels, but weights them with the inverse of the intensity variance, which, for a Poisson process, is nothing else but the pixel value itself. The software allows the simultaneous fit of several gaussians to account for nearby PSFs, as long as their respective distance is larger than a fraction of the PSF width (the exact value below which the fit fails depends on several parameters, but is generally smaller than the Rayleigh criterion for PSF separation).

4.3. Error Bar Analysis: Ideal Case

One often-overlooked problem with nonlinear minimization algorithms is that they do not directly give an estimation of the uncertainty on the fitted parameters. To estimate the uncertainty on the values obtained for a nonlinear function, several well-established methods are available, but they necessitate some extra computations. For χ^2 minimization, Bobroff has reported a formalism to derive the uncertainty on fitted parameters that relies on the assumption that the kind of noise associated with each data point is known (55). As we will see below, this assumption has to be abandoned in the case of nanocrystals. Two other popular methods are Monte-Carlo and bootstrap simulations (56). We resorted to the second, since it is easily implemented and gives rapid results (57). Briefly, this method consists of generating artificial approximate replicas of the original data set in the following way. A new set of data
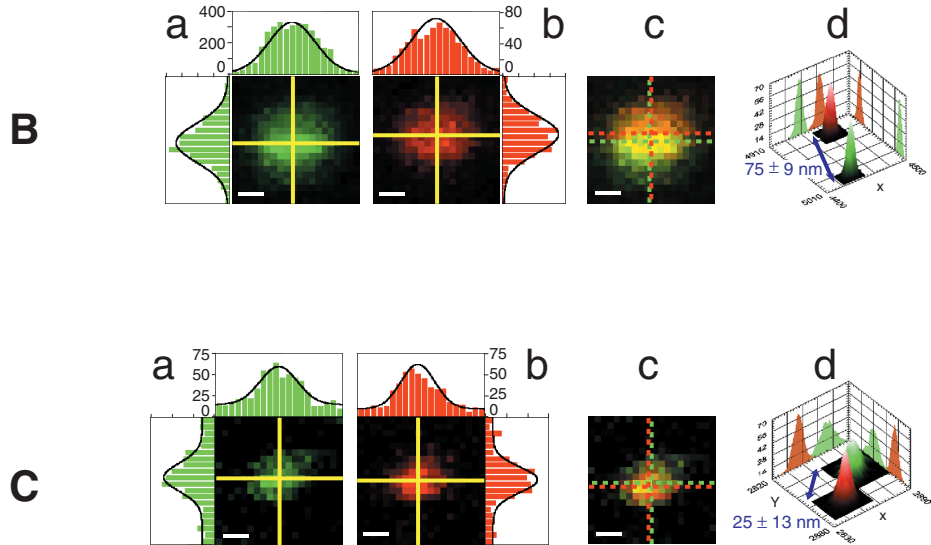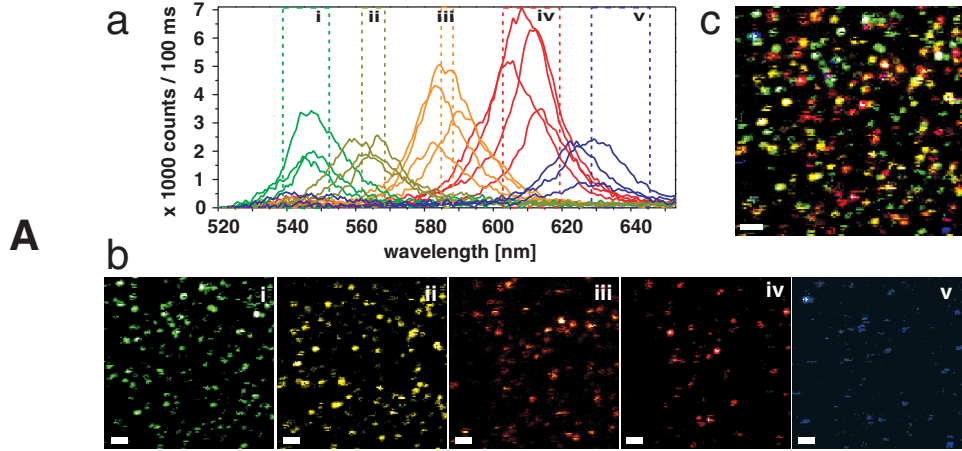
FIG. 4.   (A) Nanocrystal (NC) multicolor imaging. Scans of a mixture of four NC samples (ensemble peak emissions: 540, 575, 588, and 620 nm). (a) A representative collection of individual NC spectra (about 20 nm FWHM) obtained from the integrated data of 3×3 pixels. Despite their overlap, five "orthogonal" spectral bands (i–v) could be defined. (b) Five false-color images corresponding to the spectral bands defined in (a). (c) Overlay of the five perfectly registered images of (b); 10×10-μm^2 scan (pixel size: 78 nm, scale bar = 1 μm). (B) TransFluoSphere colocalization. Mixture of green (Em: 560 nm) and red (Em: 685 nm) TFSs excited at 488 nm (excitation power: 50 nW incident or 80 W/cm^2 peak irradiance, integration time: 10 ms). (a, b) Green and red channel images of a 1×1-μm^2 scan (pixel size: 50 nm, scale bar = 200 nm). The yellow crosses indicate the fitted PSF centers. The image intensity profiles along the two lines are represented as bar graphs; the black curve corresponds to the 2D elliptical gaussian fit. Counts are higher in the green channel than in the red, but SNR and SBR ratios are comparable. (c) Overlay of the two channels. The green and red dashed crosses indicate the centers of the green and red PSFs, respectively. From the apparent width of the PSF (990 nm), we conclude that the beads are slightly out of focus. (d) Histograms of the fitted centers of 1000 bootstrap simulations of each channel. Each probability distribution (PD) has a width of a few nanometers, corresponding to the uncertainty of the bead positions. Coordinates indicate absolute position (in nm) of the CLPS. These PDs are well fitted by 2D tilted gaussians. The calculated distance is 75 $\pm$ 9 nm (95% CL). (C) Nonblinking NC colocalization. Mixture of green (Em: 540 nm) and red (Em: 620 nm) NCs excited at 488 nm (excitation power: 200 nW incident or 320 W/cm^2 peak irradiance, integration time: 50 ms). (a, b) Green and red channel images of a 1×1-μm^2 scan (pixel size: 50 nm, scale bar = 200 nm). See caption to (B) for a general description. In this case, the count rates are similar in both channels. (c) Overlay of the two channels. (d) Histograms of the fitted center distribution. The measured distance is 25 $\pm$ 13 nm (95% CL). The precision of the measurement is comparable to that obtained for beads (B) due to negligible blinking.

points containing the same number of points as the original data set is built by randomly picking points among the list of available data points. The resulting new set has by definition the same look and feel as the original one, but a few points may be present more than once, while others will not be represented (on average, 37%). A fit performed on this new data set will thus yield a different center position. By repeating the above procedure, a distribution of fitted positions is obtained. It can be verified on simulated data that the distribution of fitted parameters has a standard variation, which is close to the actual uncertainty on the fitted parameters (computed statistically). Moreover, since repeated scans of the area can be done, we verified that the measured distances obtained from different images of the same area are in agreement within the uncertainty deduced from the bootstrap error bar analysis (37). A detailed analysis of the performed tests will be published elsewhere.

To summarize, the fitting procedure consists of: (i) delimiting the area containing the PSF of interest, (ii) performing a weighted fit of the background and PSF, (iii) performing 1000–10,000 bootstraps of the original data set and repeating the fit as many times, (iv) and extracting the uncertainties on each parameter from the resulting parameter distributions.

4.4. Setup Characterization and Error Bar Analysis

Departure from the ideal situation described previously can have many causes. For instance, defects in the laser source (power fluctuations, imperfect mode, and beam-pointing stability) will affect the shape and evolution over time of the excitation PSF. But more generally, any defect in any optical, mechanical, or electronic component of the setup may play a significant role in the final precision of the PSF image's center determination. In the following, we report on studies carried out to characterize the critical components of the acquisition setup and how we tried to control them or study the effects of their imperfections on the final result by numerical simulations. This is not withstanding specific problems arising from the sample itself. For instance, fading, blinking, and photobleaching may affect in different ways the final observed PSF shape.

4.4.1. Knowledge of the Excitation PSF

The UHRC approach is based on finding the center of the excitation volume in the sample, assuming of course that this shape does not change as the sample is scanned in the laser field transmitted by the objective. This is a good approximation in the cases studied here, but may become an overdue hypothesis in the case of nonhomogeneous, partially transparent biological samples. But of more immediate concern is the validity of fitting its shape with a 2D gaussian. It is indeed easy to check that a nonideal laser mode, or a slightly misaligned (off-axis) laser beam, or simply a defective optical component will all lead to a nonsymmetric or deformed excitation PSF. As a matter of fact, the first concern of any user of confocal microscopy should be to check the PSF shape (if possible in three dimensions), to detect any such defects. The best way to do this is by imaging a small, bright fluorescent bead, which can be considered a point-like source at the excitation wavelength (typically several times smaller than the excitation wavelength).

Strong departure from a symmetric shape is easy to detect, and often to correct, but slight departures are more subtle, in the sense that they can be hidden in the signal shot noise (which generates some kind of asymmetry of its own). Looking for higher signal-to-noise ratio is not necessarily a good idea, since it normally involves a longer integration time or larger excitation intensity, which both increase the risk of degrading the sample over time and, hence, of generating unwanted asymmetry in the excitation PSF image.

From this introductory discussion, it should be clear that three things should be checked to assess the robustness of the method: its sensitivity to slight asymmetries of the PSF; its sensitivity to changes in signal-to-noise; and its sensitivity to the photophysics of the probe (fading, blinking, etc.).

4.4.2. Effect of PSF Asymmetry

It is impossible to foresee and account for all of the aberrations in the PSF shape that may arise in a particular confocal setup. On the other hand, one can easily get an estimate of the maximal error that arises when fitting the actual PSF with a function (here a gaussian) that does not perfectly match it. To begin with, the theoretical excitation PSF of a confocal microscope is not a gaussian shape. It is not, incidentally, the famous Airy pattern either, which is valid only for the emission PSF shape of a point-like source illuminated by a uniform wide-field excitation source, or for the excitation PSF of a circularly polarized laser source in confocal microscopy.

Nevertheless, since we will rely heavily on 2D gaussian fitting, it is worth checking the quality of a fit of the Airy pattern with a 2D gaussian in the absence of noise, which will be our reference. Using the above method on simulated PSF data, it turns out that the pattern's center is perfectly determined for any pixel size up to 200 nm and any window size (number of pixels $\times$ pixel size) larger than 400 nm (we used the Airy pattern corresponding to $\lambda = 488$ nm and NA =

1.4). Moreover, there is no effect of pixelization, which means that if the pattern is digitized with a fixed pixel size, the center is perfectly determined whatever the shift of the digitization grid with respect to the pattern's center. The only noticeable problem is in the fitted amplitude of the gaussian, which departs significantly from the peak intensity for pixel sizes larger than 200 nm. However, this is information we are not interested in for colocalization studies.

If we now consider a deformed PSF (say, an elliptical one) and still fit it with a gaussian of circular symmetry, the result is essentially the same. Similar results are obtained with a tilted gaussian fitted with a gaussian of circular symmetry. Less intuitive is the case of a PSF whose intensity distribution is a gaussian modulated by a function that places emphasis on one side only (say $x > 0$). In this simulated case, illustrated in Fig. 5A, the effect is a shift of the fitted position with respect to the exact position. However, since this shift is systematic and the excitation PSF is common to all probes studied, the effect on a distance measurement cancels out, leaving only the typical standard deviation observed in the previous cases. The only caveat comes from the possible different signal-to-noise and signal-to-background ratios for the different imaged PSFs, as is discussed later. We checked that the systematic shift observed above depends neither on signal nor on background, as illustrated by numerical simulations in Figs. 5B and 5C.

The fact that a gaussian fit still makes a good job in matching an asymmetric PSF is probably due to the constraint placed on the fit by the large number of pixels of the fitted pattern. It is not within the scope of this article to discuss this fact in more detail, but it is worth knowing that it is numerically demonstrated. In summary, slight asymmetry of the experimentally observed PSF does not affect the precision of the distance measurement in our approach, because it is reproduced identically in all channels (it is the same, fixed, excitation PSF).

4.4.3. Signal-to-Background and Signal-to-Noise

Since we are working with low light levels detected by avalanche photodiodes in single-photon counting mode, a study of the sensitivity of the method to noise and background at low count rates is mandatory. The previous studies can be repeated when adding to the signal the kind of noise that is expected from the combination of using low excitation, short integration times, and APD detection, namely, shot noise. Shot noise is characterized by the fact that instead of recording a value that is proportional to the PSF value at the studied sample position, the integration time, and the APD

quantum efficiency, the recorded signal is statistically chosen out of a Poisson distribution with a mean equal to the expected value. The Poisson distribution is very similar to a gaussian distribution for mean values larger than about 100, and has a variance (square of
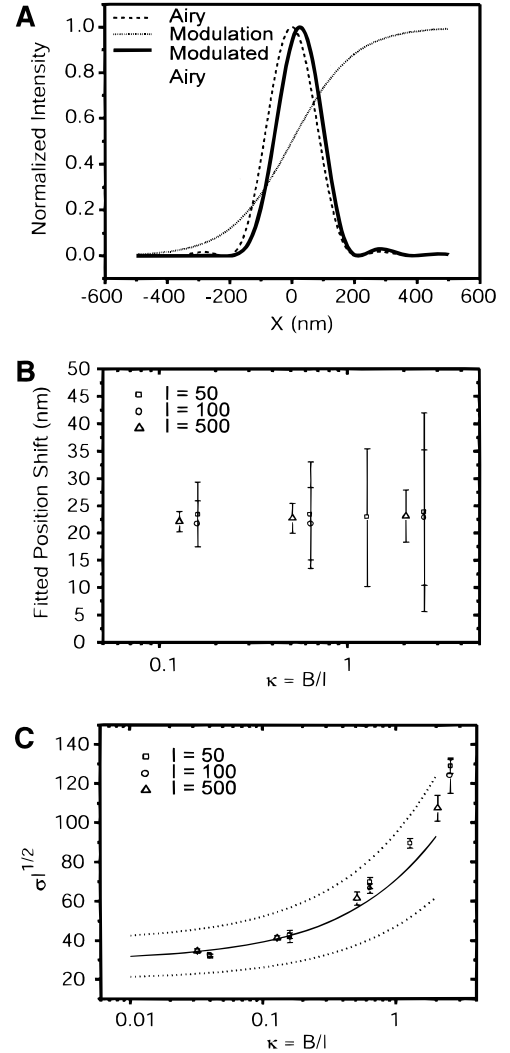

FIG. 5. (A) To study the effect of an asymmetric PSF on the reliability of the 2D Gaussian fit, we arbitrarily chose to modulate the Airy pattern ($\lambda = 488$ nm, NA = 1.4) by a 1D hyperbolic tangent function of width 200 nm along the x axis, centered on $x = 0$. As can be seen from the profile along $y = 0$, the effect is to shift the peak position and to suppress one side of the lobes ($x < 0$). (B) Measured shift along the x axis (in nm) as a function of background-to-signal ratio for different signal values I (in counts per pixel). Each point and error bar correspond to the mean and standard deviation of 1000 simulations and fits of an Airy pattern centered at the origin. Each image contains 20 × 20 pixels of size 50 nm. (C) Evolution of the normalized uncertainty $\sigma I^{1/2}$ as a function of background-to-signal ratio $\kappa = B/I$ for different signal values. The curves correspond to 1, 1.5, and 2 times the expected error bar for a perfect Airy pattern fitted by the χ^2 method.

the standard deviation) equal to its mean value. Since there is only one readout per pixel during each scan, the resulting PSF image will have a noisy aspect, and the fitted center's position will be affected. In principle, multiple scanning and averaging of the same PSF can reduce the shot noise, but at the same time it will increase the probability for photobleaching.

If we first suppose that there is no background signal, fitted numerical simulations of PSFs with varying peak values exhibit a position uncertainty which scales like the inverse of the signal's standard deviation, as illustrated in Fig. 6. This is the expected behavior, checked here for our fitting approach. However, it is difficult to completely get rid of background signal, which may have several sources: thermal noise of the APD (dark noise limited to less than 1 kHz in our experiments), Rayleigh scattering of the excitation light or autofluorescence of the coverslip, and imperfect alignment or choice of pinhole are the most common. A similar study of the performance of the fitting approach requires choosing a signal level I above background B (and, of course, fixed pixel size δx and window size $N\delta x$) and generating a statistically significant number of simulated PSFs for different background levels B. The results of such a study are shown in Fig. 7A, where data for different background and signal levels have been rescaled to a universal curve. The statistical uncertainty in the center's position σ is relatively insensitive to the signal-to-background level I/B when this one is large, but rises when it falls below 5–10. It is related to the previous parameters by

$$\sigma = (\pi I)^{-1/2} g_3 (B/I) \delta x, \qquad [1]$$

where

$$g_i(\kappa) = \left(\int_0^\infty du \, \frac{u^i e^{-u^2}}{\kappa + e^{-u^2/2}} \right)^{-1/2}. \qquad [2]$$

and $\kappa = B/I$ is the background-to-signal ratio. Equation [1] is specific to the 2D case and can be derived using a formalism similar to that used by Bobroff (55). In particular, it is important to note that the uncertainty depends on the signal-to-background ratio (SBR = I/B), the signal-to-noise ratio (SNR = $I/(I + B)^{1/2}$), and
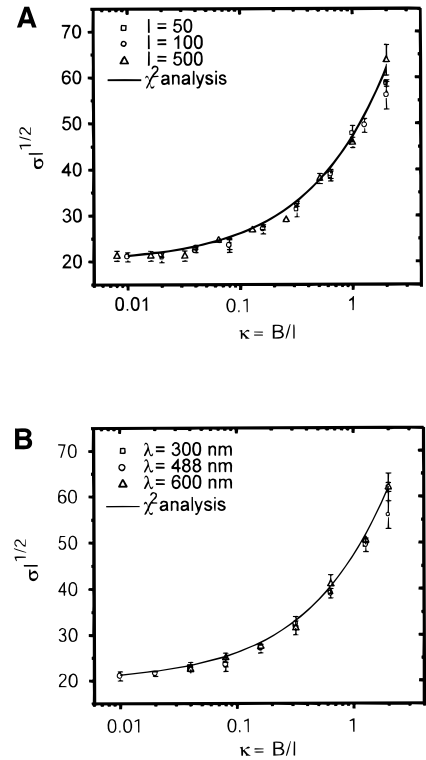
FIG. 7. (A) Normalized uncertainty $\sigma I^{1/2}$ as a function of background-to-signal ratio $\kappa = B/I$ for different signal values (simulated data). All curves fall on the theoretical uncertainty obtained by χ^2 minimization. (B) Normalized uncertainty $\sigma I^{1/2}$ as a function of background-to-signal ratio $\kappa = B/I$ (simulated data) for different Airy pattern diameter (equivalently, different wavelengths). The common peak intensity in these simulation is $I = 100$ counts per pixel (cpp). As is expected for a 2D fit using a χ^2 minimization procedure, all data points fall on a universal curve. This is in marked distinction to the 1D case, where the uncertainty also depends on the width of the gaussian. In both cases, each point and error bar corresponds to the mean and standard deviation of 1000 simulations and fits of an Airy pattern centered at the origin. Each image contains 20 × 20 pixels of size 50 nm.

FIG. 6. Uncertainty σ in the fitted center's position (in nm) as a function of peak signal I (in counts per pixel) in the absence of background (simulated data). The line is a power law fit yielding an exponent of -0.48 ± 0.1 in agreement with expectation. Each point corresponds to the mean of 1000 simulations and fits of an Airy pattern centered at the origin. Each image contains 20 × 20 pixels of 50 nm.

the signal level,[4] as well as on the pixel size, but not on the PSF width, as illustrated in Fig. 7B.[5]

In summary, signal-to-background and signal-to-noise should be maximized, with priority to signal-to-noise.

4.4.4. Effect of the Uncertainty in Stage Position

A crucial point of UHRC is the knowledge of the respective position of the sample and the center of the excitation PSF, for each pixel or data point. This is possible due to the precision of the piezo-stage used for the sample displacement, in opposition, for instance, to a beam-scanning system. However, this knowledge depends on the reliability of the position measurement of the closed-loop piezo-scanner. The nominal precision of the capacitive sensor goes down to a few femtometers, but the actual precision achievable by the piezo-device is not as good and depends on mechanical factors (mechanical stability of the whole mount, thermal stability, etc.) and electronic factors. The manufacturer certifies a 1-nm resolution in the positioning of the scanner if used under proper conditions. However, the actual motion of the stage is not an instantaneous and oscillation-free process; in fact, there are observable oscillations from the position recording, whose exact amplitude, damping, and overall duration depend on the electronic settings and the step instruction sent to the stage. For instance, our stage was factory-tuned to reach the steady-state set-point value as fast as possible (with a small overshoot, slightly faster than a critically damped response) for 100-nm steps. This response time to steady state is typically reached after ~10 ms. For different settings (larger steps or faster update), detrimental effects like mechanical ringing may affect the precision of the stage positioning.

In addition to these effects, the position information is read by an electronic system, which can itself be contaminated by noise. For instance, we should take into account the digitization noise of the data acquisition board, possible contamination of the signal by ground-loop noise, etc. Altogether, these phenomena lead to an uncertainty in the exact position of the sample that is far larger than the factory-quoted precision of the stage (1 nm), as illustrated by actual recordings in Figs. 8A and 8B. We decided to study the effect of these perturbations on the precision of the PSF image formation and PSF center determination, by simulating data that were generated for a sample moved along in a similar way (using actual recorded position files). The
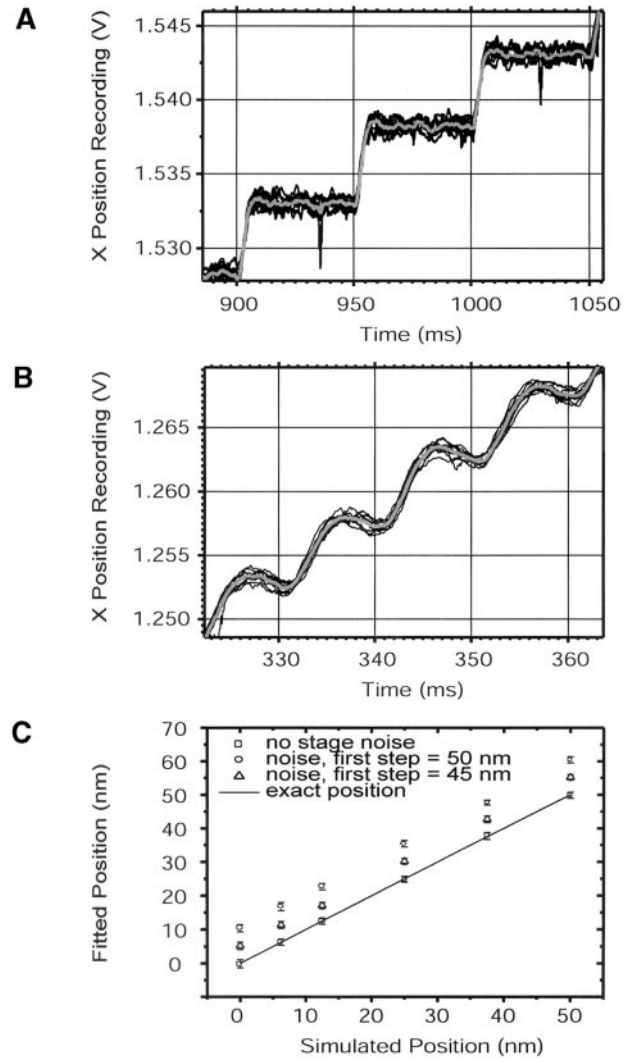

FIG. 8. X position recording from the piezo-stage's capacitive sensor. The signal (0–10 V) was recorded at 10 kHz with a 12-bit digitization board (PCI 6111E, National Instruments). (A) Part of a 2×2-μm^2 scan, 50-nm step, 50 ms per pixel. Some "glitches" correspond to parasites from the laser power supply, whereas the overall fluctuations correspond to an untreated ground-loop noise (1-mV amplitude). The rise time is less than 10 ms. (B) Part of a 5×5-μm^2 scan, 50-nm step, 10 ms per pixel. In this case, the rise time is of the order of the pixel integration time, so no stable equilibrium is reached: a slight overshoot can be noted. In both cases, the signals of 10 lines are overlaid, the thick gray curve representing their average. The grid is a guide for the eyes and indicates the step size and pixel duration. These very signals were used to generate simulations of recorded PSF images to check their influence on the fitting accuracy. (C) Fitted X position as a function of the true PSF position, using an X position file similar to the above ones. To take into account the uncertainty in the definition of a "step" position for a non-square stair pattern, different values were used to study the influence of this uncertainty (the best-fit value is obtained by fitting the histogram of recorded positions with equidistant gaussian peaks, of a few nanometers' width). The fitted position is determined with the same accuracy as in the absence of piezo-stage noise. Simulation parameters: pixel size = 50 nm, area width = 40 pixels, $I = 100$ cpp, no background.

---

[4] The dependence on the SNR is simple only in the case of low background, in which SNR $\sim I^{-1/2}$.

[5] Of course, formula [1] is valid only as long as the Nyquist criterion is verified.

results are displayed in Fig. 8C. It can be seen that the precision of the fit is not affected by these additional uncertainties, due to their systematic nature. Nevertheless, it is important to check them systematically, a reason that led us to continuously record the position of the stage (at 10 kHz).

4.5. Uncertainty on Distance Measurement

We have seen that it is relatively easy to define a specific uncertainty for each observed PSF (as opposed to a common, statistical uncertainty, as is often used in the literature), via the probability distribution obtained by bootstrap simulations. The uncertainty in the distance between the two centers of the fitted PSFs should reflect the two different probability distributions of the PSF positions. It turns out that the corresponding probability distribution can be computed analytically after some lengthy algebra, assuming that the two PSF probability distributions are tilted, elliptical 2D gaussians. Armed with this function, it is then easy to compute the uncertainty in the distance measurement between two PSFs from the parameters of the distribution of their bootstrapped, fitted centers. For typical error bars small compared with the distance, the resulting probability distribution is nearly gaussian. As a result, we usually quote the more stringent 95% confidence level values for the error bar (the 2σ interval of a gaussian probability distribution).

5. RESULTS

We now report results obtained with the above experimental setup and analysis approach for two different model fluorescent probes. These data have already been presented in a brief letter format in Ref. (37).

5.1. TransFluoSphere Beads

TFSs are carboxylate-modified polystyrene beads loaded with a series of two or more dyes having overlapping emission and excitation spectra. Energy transfer between each pair of spectrally overlapping dyes results in large Stokes shifts so that only the longest-wavelength dye exhibits significant fluorescence. We tested four types of TFSs (40 nm diameter) excited at 488 nm with emission peaks centered at 560, 605, 645, and 685 nm (47 nm FWHM). In our dual-color analysis, we used the two extreme colors to minimize spectral overlap between the detectable emissions, i.e., the 560- and 685-nm beads. Although containing hundreds of dye molecules per bead, noticeable photobleaching was still

observed for the 685-nm TFSs, but only after several minutes of continuous excitation. Incident laser excitation power was kept at 50 nW (80 W/cm² peak irradiance), maintaining acceptable SNR and reasonable photostability during the acquisition of the image.

Figure 4B gives an example of colocalization data obtained with TFSs for 50-nm pixels. The two separate color planes (Fig. 4B, parts a and b) show very similar positions for the slightly elliptical PSFs, but the composite image (Fig. 4B, part c) exhibits a slight but discernible shift between the two: the measured distance between the two beads' centers is 75 ± 9 nm. Figure 4B, part d, shows the probability distribution for each PSF coordinate as derived from the bootstrap calculations.

This result is typical of what we obtained with the TFSs at this excitation power and with this pixel size. The uncertainty is essentially due to the shot noise emission of the beads and to the background noise level, as checked by numerical simulations. The green beads gave a maximum signal on the order of $I_1 + B_1 = 400$ counts per pixel (cpp) (integration time: 10 ms), whereas the red signal was lower than $I_2 + B_2 = 100$ cpp. However, the background signal was larger in the green channel ($B_1 = 20$ cpp) than in the red ($B_2 = 5$ cpp), resulting in similar SNR ($\text{SNR}_1 = 19$, $\text{SNR}_2 = 9.5$) and SBR ($\text{SBR}_1 = \text{SBR}_2 = 19$) and, hence, similar uncertainties in the fit.

5.2. Nanocrystals

NCs are small semiconductor nanocrystalline objects with diameters that can be fine-tuned from 2 to 10 nm. Their absorption edge and emission peak scale with size due to quantum confinement. The emission wavelength can be tuned by means of material composition and NC size anywhere from the ultraviolet to the infrared (42). For the experiments described here, we used CdSe/ZnS core-shell NCs with emission peaks between 540 and 620 nm, and a typical ensemble solution FWHM of 30 nm. NCs are brighter (depending on excitation conditions) than their organic dye counterparts and, live longer, but suffer from intermittent fluorescence emission (resulting in "blinking") (58–61). They exhibit dark states that can span any duration from microseconds to seconds, sometimes accompanied by intermittent spectral jumps (62). This photophysical behavior can result in a strong nonlinear relationship between the laser excitation power and the fluorescence emission.

Practically, when trying to map the excitation PSF with a NC by scanning, the outcome can be in the worst cases a patchy PSF image with no obvious relation between the excitation intensity and the integrated emission intensity. As a result, some PSFs appear as if the

source bleached during the scanning, reducing the number of pixels for the fit, and more generally have an irregular shape that significantly reduces the precision of localization. However, since NCs can be synthesized in a larger number of well-separated colors, they are extremely attractive for applications that need multicolor detection. This is illustrated in Fig. 4A with a mixture of four different NC colors using the multicolor scanning-stage confocal setup. Although only four NC batches were used, spectral analysis of the sample revealed five distinct spectral peaks (the batch with nominal 620-nm peak showed a bimodal distribution) as indicated by different colors in Fig. 4A, part a. Accordingly, five bands were defined (marked i through v) and five different false-color images were generated (Fig. 4A, part b). Their overlay is shown in Fig. 4A, part c. Noteworthy is the "black stripe" pattern of several PSFs, corresponding to long dark states.

Figure 4C illustrates a simpler case of a NC pair prepared from two different NC batches and observed with the APD detection and closed-loop scanner setup. Figure 4C shows a 1×1-μm^2 region (50-nm pixel size, 200-nW or 320-W/cm^2 peak irradiance, 50-ms integration time), containing two NCs (540 and 620 nm) used for ultrahigh-resolution measurements. Due to minimal blinking during this scan, the distance measurement (25 ± 13 nm, 95% CL) exhibits a precision similar to that of the TFSs.

More often, blinking severely affects the PSF shape, resulting in larger error bars on the center's position. In particular, images of the same area scanned repeatedly may yield different estimations of the distance between the observed nanocrystals (see Ref. (37)).

The effect of NC intermittency on the precision of PSF fit was simulated by numerical simulations, assuming either an exponential or a power-law distribution of dark (off) and emitting (on) intervals, since both are experimentally observed (60, 61; our unpublished observations). Other maximum-likelihood fitting methods might slightly improve the results, but in many cases of observed blinking patterns, they will also face similar limitations as the χ^2 minimization method.

The previous data illustrate advantages and limitations of TFSs versus NCs. As discussed in the literature (55) and in the previous sections, the precision in both cases is affected by three factors: SNR, SBR, and pixel size. The pixel size could easily be decreased, but scan time would correspondingly increase if the same SNR and SBR were kept.

We found out that a pixel size of 50 nm resulting in a 95% CL error bar of about 10 nm is a good trade-off. It is indeed of doubtful utility to increase much more the localization accuracy of objects having diameters larger than 10 nm (like TFS beads) or comparable to

it (like NCs). These probes will ultimately be used to report the presence of nonfluorescent molecules (e.g., proteins) whose attachment position onto the probe's surface will remain unknown. Hence, with this choice of pixel size, resolution is limited only by the size of the reporter.

6. CONCLUSION AND PERSPECTIVES

The UHRC method described in this article has been validated and proved reliable for measuring distances ranging from a few nanometers to many micrometers. The noninvasiveness, nanometer molecular accuracy, and large dynamic range (bridging FRET distances with conventional far-field imaging) make this method very attractive for high-resolution molecular imaging in live cells.

So far, the method has been used on 2D model systems (randomly distributed single fluorescent beads or nanocrystals on a flat surface). It is thus perfectly adapted to high-resolution mapping of fluorescently labeled genes or DNA-binding proteins on DNA stretched on glass surfaces (63). We are currently developing this application.

More recently, we applied the UHRC approach to conventional, smaller beads (20 nm in diameter) filled with standard dyes. To efficiently excite different dyes with a common excitation, we used two-photon excitation (Tsing-Hua Her *et al.*, submitted). The only difference from the discussion above is the shape of the excitation PSF, which is now the square of the one-photon excitation. It can be shown that this shape is also efficiently fitted by a 2D gaussian, so that the exact same procedure can be used to extract position and distance uncertainties from colocalized beads. Two of the advantages of two-photon excitation are the intrinsic background rejection and the possibility of using a variety of standard dyes. In the future, we will investigate single-molecule ultrahigh-resolution colocalization using two-photon excitation. This should be feasible if conditions are found that prevent bleaching of the dyes before a large enough part of the PSF has been acquired (32, 64).

UHRC could readily be extended to 3D colocalization, a field where several techniques have been developed to try to account for chromatic and other aberrations (21–24, 54). However, these methods lack the complete elimination of chromatic aberrations in the excitation and the detection paths. In fact, in the 3D case, the resolving power of our method should increase significantly due to the larger number of 3D PSF data points involved in the fitting. Several counterbalancing factors will have to be considered: longer acquisition time,

which might lead to premature bleaching of the probes and to noticeable thermal drift of the stage support; PSF asymmetry due to index mismatch; and polarization effects at optical interfaces should all be carefully studied. Finally, the time needed to acquire sufficient stacks of 2D scans to reach a reasonable resolution might become prohibitory in the stage-scanning approach. Investigation of the same UHRC approach using beam-scanning confocal microscopy (which is prone to off-axis optical aberrations and less controllable stepping resolution, accuracy, and repeatability) might allow quicker 3D scanning. The improved scanning rate, however, will be limited by the signal-to-noise ratio of the final signal.

Ultimately, we envision the development of unique fluorescent reagents, optical methods, and instrumentation that allow ultrahigh-resolution, ultrahigh-sensitivity, multiplexed detection of individual molecules/molecular complexes interacting in live cells.

ACKNOWLEDGMENTS

REFERENCES

1. Gibson, S. F., and Lanni, F. (1989). *J. Opt. Soc. Am. A* 6, 1357–1367.

2. McNally, J. G., Karpova, T., Cooper, J., and Conchello, J. A. (1999) *Methods* 19, 373–385.

3. Carrington, W. A., Lynch, R. M., Moore, E. D. W., Isenberg, G., Fogarty, K. E., and Fay, F. S. (1995) *Science* 268, 1483–1487.

4. Rizzuto, R., Pinton, P., Carrington, W., Fay, F. S., Fogarty, K. E., Lifshitz, L. M., Tuft, R. A., and Pozzan, T. (1998) *Science* 280, 1763–1766.

5. Scalettar, B. A., Swedlow, J. R., Sedat, J. W., and Agard, D. A. (1996) *J. Microsc.* 182, 50–60.

6. Lanni, F., Bailey, B., Farkas, D. L., and Taylor, D. L. (1993) *Bioimaging* 1, 187–196.

7. Gustafsson, M. G. L., Agard, D. A., and Sedat, J. W. (1999) *J. Microsc.* 195, 10–16.

8. Frohn, J. T., Knapp, H. F., and Stemmer, A. (2000) *Proc. Natl. Acad. Sci. USA* 97, 7232–7236.

9. Cragg, E. G., and So, P. T. (2000) *Opt. Lett.* 25, 46–48.

10. Hegedus, Z. S., and Sarafis, V. (1986) *J. Opt. Soc. Am. A* 3, 1892–1896.

11. Schmidt, T., Schütz, G. J., Baumgartner, W., Gruber, H. J., and Schindler, H. (1996) *Proc. Natl. Acad. Sci. USA* 93, 2926–2929.

12. Schütz, G. J., Pastushenko, V. P., Gruber, H. J., Knaus, H.-G., Pragl, B., and Schindler, H. (2000) *Single Molecules* 1, 25–31.

13. Gelles, J., Schnapp, B. J., and Sheetz, M. P. (1988) *Nature* 331, 450–453.

14. Verveer, P. J., and Jovin, T. M. (1997) *J. Opt. Soc. Am. A* 14, 1696–1706.

15. Conchello, J. A., and Hansen, E. H. (1990) *Appl. Opt.* 29, 3795–3804.

16. Hell, S., and Stelzer, E. H. K. (1992) *J. Opt. Soc. Am. A* 9, 2159–2166.

17. Klar, T. A., and Hell, S. W. (1999) *Opt. Lett.* 24, 954–956.

18. Klar, T. A., Jakobs, S., Dyba, M., Egner, A., and Hell, S. W. (2000) *Proc. Natl. Acad. Sci. USA* 97, 8206–8210.

19. Denk, W., Piston, D. W., and Webb, W. W. (1995) *in* Handbook of Biological Confocal Microscopy (Pawley, J. B., Ed.), pp. 445–458, Plenum, New York.

20. Keller, H. E. (1995) *in* Handbook of Biological Confocal Microscopy (Pawley, J. B., Ed.), pp. 111–126, Plenum, New York.

21. Patwardhan, A., and Manders, E. M. M. (1996) *Bioimaging* 4, 17–24.

22. Manders, E. M. M. (1997) *J. Microsc.* 185, 321–328.

23. Edelman, P., Esa, A., Hausmann, M., and Cremer, C. (1999) *Optik* 110, 194–198.

24. Edelman, P., and Cremer, C. (2000) *in* Optical Diagnostics of Living Cells III, SPIE, Vol. 3921, pp. 313–320.

25. Synge, E. H. (1928) *Philos. Mag.* 6, 356.

26. O'Keefe, J. A. (1956) *J. Opt. Soc. Am.* 46, 359.

27. Lewis, A., Isaacson, A., Harootunian, A., and Muray, A. (1984) *Ultramicroscopy* 13, 227–230.

28. Pohl, D. W., Denk, W., and Lanz, M. (1984) *Appl. Phys. Lett.* 44, 651.

29. Inouye, Y., and Kawata, S. (1994) *Opt. Lett.* 19, 159–61.

30. Zenhausern, F., Oboyle, M. P., and Wickramasinghe, H. K. (1994) *Appl. Phys. Lett.* 65, 1623–1625.

31. Zenhausern, F., Martin, Y., and Wickramasinghe, H. K. (1995) *Science* 269, 1083–1085.

32. Sánchez, E. J., Novotny, L., Holtom, G. R., and Xie, S. X. (1997) *J. Phys. Chem. A* 101, 7019–7023.

33. Sánchez, E. J., Novotny, L., and Xie, X. S. (1999) *Phys. Rev. Lett.* 82, 4014–4017.

34. Eckert, R., Freyland, J. M., Gersen, H., Heinzelmann, H., Schürmann, G., Noell, W., Staufer, U., and de Rooij, N. F. (2000) *Appl. Phys. Lett.* 77, 3695–3697.

35. Dunn, R. C. (1999) *Chem. Rev.* 99, 2891–2927.

36. Weiss, S. (1999) *Science* 283, 1676–1683.

37. Lacoste, T. D., Michalet, X., Pinaud, F., Chemla, D. S., Alivisatos, A. P., and Weiss, S. (2000) *Proc. Natl. Acad. Sci. USA* 97, 9461–9466.

38. Ha, T., Enderle, T., Chemla, D. S., and Weiss, S. (1996) *IEEE J. Selected Top. Quantum Electronics* 2, 1115–1128.

39. Enderle, T., Ha, T., Ogletree, D. F., Chemla, D. S., Magowan, C., and Weiss, S. (1997) *Proc. Natl. Acad. Sci. USA* 94, 520–525.

40. Enderle, T., Ha, T., Chemla, D. S., and Weiss, S. (1998) *Ultramicroscopy* 71, 303.

41. Betzig, E. (1995) *Opt. Lett.* 20, 237–239.

42. Alivisatos, A. P. (1996) *Science* 271, 933–937.

43. Bruchez, M. J., Moronne, M. M., Gin, P., Weiss, S., and Alivisatos, P. A. (1998) *Science* 281, 2013–2016.

44. Chan, W. C. W., and Nie, S. (1998) *Science* 281, 2016–2018.

45. Ju, J., Ruan, C., Fuller, C. W., Glazer, A. N., and Mathies, R. A. (1995) *Proc. Natl. Acad. Sci. USA* 92, 4347–4351.

46. Tinnefeld, P., Buschmann, V., Herten, D.-P., Han, K.-T., and Sauer, M. (2000) *Single Molecules* 1, 215–223.

47. Xu, C., Zipfel, W., Shear, J. B., Williams, R., and Webb, W. W. (1996) *Proc. Natl. Acad. Sci. USA* 93, 10763–10768.

48. Mertz, J., Xu, C., and Webb, W. W. (1995) *Opt. Lett.* 20, 2532–2534.

49. Burns, D. H., Callis, J. B., Christian, G. D., and Davidson, E. R. (1985) *Appl. Opt.* 24, 154–161.

50. Betzig, E., Trautman, J. K., Harris, T. D., Weiner, J. S., and Kostelak, R. L. (1991) *Science* 251, 1468–1470.

51. Peng, X. G., Schlamp, M. C., Kadavanich, A. V., and Alivisatos, A. P. (1997) *J. Am. Chem. Soc.* 119, 7019–7029.

52. Cogswell, C. J., and Larkin, K. G. (1995) *in* Handbook of Biological Confocal Microscopy (Pawley, J. B., Ed.), pp. 127–137, Plenum, New York.

53. Warner, I. M., Christian, G. D., Davidson, E. R., and Callis, J. B. (1977) *Anal. Chem.* 49, 564–573.

54. Kubitscheck, U., Kues, T., and Peters, R. (1999) *in* Confocal Microscopy (Conn, P. M., Ed.), Vol. 307, pp. 207–230, Academic Press, San Diego.

55. Bobroff, N. (1986) *Rev. Sci. Instrum.* 57, 1152–1157.

56. Press, W. H., Teukolsky, S. A., Vetterling, W. T., and Flannery, B. P. (1996) Numerical Recipes in C: The Art of Scientific Computing, Cambridge Univ. Press, London/New York.

57. Efron, B., and Tibshirani, R. J. (1994) An Introduction to the Bootstrap, CRC Press, Boca Raton, FL.

58. Nirmal, M., Dabbousi, B. O., Bawendi, M. G., Macklin, J. J., Trautman, J. K., Harris, T. D., and Brus, L. E. (1996) *Nature* 383, 802–804.

59. Efros, A. L., and Rosen, M. (1997) *Phys. Rev. Lett.* 78, 1110–1113.

60. Banin, U., Bruchez, M., Alivisatos, A. P., Ha, T., Weiss, S., and Chemla, D. S. (1999) *J. Chem. Phys.* 10, 1–7.

61. Kuno, M., Fromm, D. P., Hamann, H. F., Gallagher, A., and Nesbitt, D. J. (2000) *J. Chem. Phys.* 112, 3117–3120.

62. Neuhauser, R. G., Shimuzu, K. T., Woo, W. K., Empedocles, S. A., and Bawendi, M. G. (2000) *Phys. Rev. Lett.* 85, 3301–3304.

63. Michalet, X., Ekong, R., Fougerousse, F., Rousseaux, S., Schurra, C., Hornigold, N., Slegtenhorst, M. V., Wolfe, J., Povey, S., and Bensimon, A. (1997) *Science* 277, 1518–1523.

64. Heinze, K. G., Koltermann, A., and Schwille, P. (2000) *Proc. Natl. Acad. Sci. USA* 97, 10377–10382.

65. van Oijen, A. M., Köhler, J., Schmidt, J., Müller, M., and Brakenhoff, G. J. (1998) *Chem. Phys. Lett.* 292, 183–187.

66. van Oijen, A. M., Köhler, J., Schmidt, J., Müller, M., and Brakenhoff, G. J. (1999) *J. Opt. Soc. Am. A* 16, 909–915.